Design of the Image Rejection Filter for Fusion Millimeter-wave Diagnostics

Khadija Rahman[1], Xiaoliang Li[1*], Pengjun Sun[2], Shasha Qiu[1], Logan Himes[1], Calvin Domier[1], Hsiangying Lai[1,3], Xinhang Xu[1], Baron Li[1], and Yilun Zhu[1]

[1] *University of California Davis, Davis, California, 95616, USA*

[2] *Institute of Plasma Physics, Chinese Academy of Sciences, Hefei, Anhui, 230031, People's Republic of China*

[3] *National Yang Ming Chiao Tung University, Hsinchu, 300093, Taiwan*

E-mail: *bxlli@ucdavis.edu*

Millimeter-wave diagnostics are essential for the safety monitoring of fusion reactors and typically utilize single-sideband heterodyne detection, which requires high-performance image rejection filters. For integration into fusion reactor diagnostics, these filters must be highly compact and robust. This paper presents a waveguide-based (WR-10) 6-order W-band image rejection filter for the Collective Thomson Scattering receiver system in the burning plasma device. The filter is designed using an advanced synthesis method to achieve a sharp drop-off and high rejection. It exhibits a passband of 100 – 110 GHz with an insertion loss of < 1 dB and provides > 40 dB rejection depth in the image band (86 – 96 GHz). Furthermore, the design features a compact form factor, essential for integration into the constrained spaces of diagnostic port plugs. In addition, we demonstrate that this design approach is scalable to the D-band (WR-06), with simulated results confirming comparable performance, thereby offering a viable and future-proof solution for advanced diagnostics in next-generation, high-magnetic-field fusion devices and compact tokamaks.

Section 1: Introduction

The pursuit of magnetic confinement fusion as a viable energy source demands sophisticated diagnostic tools to probe the extreme conditions within high-temperature plasmas[1][2][3]. Among these, millimeter-wave (mm-wave)[7][8][9] and terahertz (THz) diagnostics[6] have become indispensable, utilizing both active and passive methods to provide essential measurements of essential parameters such as electron density[7][8][9], temperature[10][11][12][13], magnetic field dynamics[14], and particle velocity distributions[15]. The evolution of these diagnostics is being propelled by cutting-edge technologies, including system-on-chip (SoC) semiconductor integrated circuits[16][17][18], synthetic diagnostic modeling[19][20][21][22], AI-assisted prediction of plasma instabilities[23], and real-time feedback control[24][25]. These advancements are enhancing our ability to understand and control plasma behavior, pushing the frontiers of fusion research.

A quintessential example of these advanced diagnostics is millimeter-wave Collective Thomson Scattering (CTS)[26]. This technique is uniquely capable of measuring ion temperature, ion velocity distribution, and fast-ion populations in the challenging environment of burning plasmas. CTS operates by directing a high-power, coherent millimeter-wave beam into the plasma. The beam is scattered by collective fluctuations in the electron density, which are intrinsically coupled to the ion dynamics. By analyzing the spectrum of this scattered radiation, CTS provides invaluable, localized insights into ion kinetics and plasma microturbulence, data that is critical for validating theoretical models and optimizing heating and confinement scenarios.

This work focuses on the development of a major subsystem for a specific CTS receiver designed to capture scattered signals in the 100 – 110 GHz frequency band as shown in Fig.1. The receiver employs a superheterodyne architecture, using a 98 GHz local oscillator (LO) to down-convert the high-frequency signals to a more manageable intermediate frequency (IF). While this architecture is chosen for its high sensitivity, it introduces a significant challenge: inherent susceptibility to interference from the image frequency band. For the given LO, this image band resides at 86 – 96 GHz. Any spurious signal or noise within this range is down-converted to the same IF as the desired signal, potentially corrupting the fragile scattering spectrum and compromising the accuracy of the derived physical parameters. To ensure signal integrity and measurement accuracy, it is therefore imperative to implement a high-performance image rejection filter at the receiver's front-end [27]. This band-pass filter must exhibit a sharp roll-off and a rejection depth greater than 40 dB to effectively attenuate these spurious image signals, thereby significantly improving the system's signal-to-noise ratio and overall sensitivity. The design of such a filter for this frequency range presents a distinct set of engineering challenges.

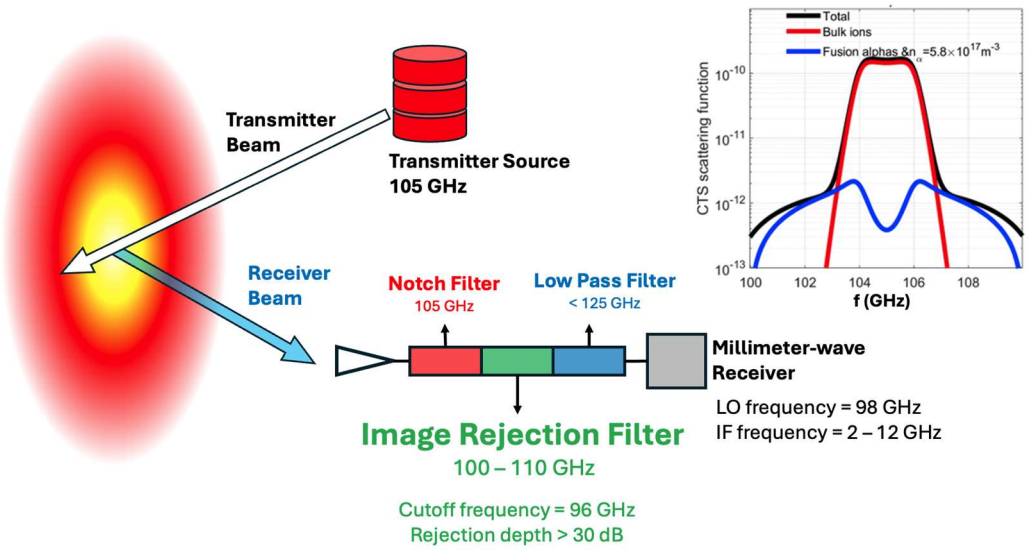

Figure 1. Diagram of the millimeter-wave Collective Thomson Scattering system, with 105 GHz transmitter source, and W-band receiver system (primary working frequency at 100 -110 GHz). As shown in the simulated scatting spectrum, the red line stands for bulk ions scattering

components. The blue line stands for alpha particle scattering components. There are 3-stage millimeter-wave front-end filters, including 105 GHz notch filter, image rejection filter with 100 – 110 GHz pass band, and low pass filter with 125 GHz cutoff frequency.

The band-pass filters discussed in this work are specified and designed to meet the stringent requirements of the CTS receiver. The remainder of this paper is structured as follows. Section II will detail the fundamental principles and methodology behind the filter design. Section III will present and compare the simulated performance. Finally, in Section IV, we demonstrate that this design approach is scalable to the D-band (WR-06, 110 - 170 GHz), with simulated results confirming comparable performance. This scalability underscores the viability of the proposed design as a future-proof solution for next-generation advanced plasma diagnostics.

Section 2: Principle of waveguide Bandpass Filter

Waveguide bandpass filters are widely employed in millimeter-wave and terahertz systems due to their inherently low insertion loss, high power handling capability, and excellent electromagnetic shielding. In rectangular waveguides, only transverse electric and transverse magnetic modes can propagate, and the dominant TE10 mode is typically selected for filter design. By introducing discontinuities or resonant sections along the propagation direction, frequency-selective characteristics can be realized. In this work, the bandpass filter is implemented using a cascaded waveguide resonator configuration [28][29], where each resonator operates near its fundamental TE101resonance mode. The collective response of multiple coupled resonators forms the desired bandpass behavior with sharp roll-off and high rejection characteristics.

To achieve a well-controlled passband response, a Chebyshev-like filtering function is adopted [30]. Compared with Butterworth filters, Chebyshev filters exhibit a ripple in the passband but provide a much steeper attenuation slope near the band edges, which is crucial for high image rejection in heterodyne fusion diagnostics receivers. The Chebyshev filter is synthesized using the insertion loss method, where the power loss ratio is defined as a function of Chebyshev polynomials. By specifying the allowable passband ripple and required out-of-band attenuation, the minimum filter order can be determined. The normalized low-pass prototype with unit cutoff frequency and source impedance is first established, serving as the foundation for the subsequent physical waveguide realization. For reference, Table I lists some element values for Chebyshev LP-prototype filters with a passband ripple of 0.5 dB[30].

Table I. Element values for Nth order Chebyshev LP prototype filter with normalized input impedance g_0 = 1Ω, cut off frequency Ω_c = 1 Hz and passband ripple L_{Ar} = 0.5 dB

N	g_1	g_2	g_3	g_4	g_5	g_6	g_7	g_8	g_9	g_{10}
1	0.6986	1								

2	1.4029	0.7071	1.9841							
3	1.5963	1.0967	1.5963	1						
4	1.6703	1.1926	2.3661	0.8419	1.9841					
5	1.7058	1.2296	2.5408	1.2296	1.7058	1				
6	1.7254	1.2479	2.6064	1.3137	2.4758	0.8696	1.9841			
7	1.7372	1.2583	2.6381	1.3444	2.6381	1.2583	1.7372	1		
8	1.7451	1.2647	2.6564	1.359	2.6964	1.3389	2.5093	0.8796	1.9841	
9	1.7504	1.269	2.6678	1.3673	2.7239	1.3673	2.6678	1.269	1.7504	1

The transformation from the low-pass prototype to a bandpass filter is accomplished through standard frequency and impedance scaling. Each series inductor and shunt capacitor in the low-pass prototype is replaced by a series or parallel LC resonant circuit that resonates around the desired center frequency. This lowpass to bandpass transformation introduces two critical design parameters: the center angular frequency ω_0 and the fractional bandwidth Δ. The values of the new circuit components can be found by scaling the frequency domain as described in equations (1) and (2):

$$\omega \rightarrow \omega' = \frac{1}{\Delta}\left(\frac{\omega}{\omega_0} - \frac{\omega_0}{\omega}\right) \quad (1)$$

$$\Delta = \frac{\omega_2 - \omega_1}{\omega_0} \quad (2)$$

ω_1 and ω_2 are the angular frequencies of the lower and higher passband edges, corresponding to the desired frequency response. The center frequency ω_0 is defined as the geometric mean $\sqrt{\omega_1\,\omega_2}$. Based on the required attenuation at ω_1 and ω_2, together with the relationship between the filter attenuation and the normalized frequency [31], the required filter order (N) can be determined. The resulting resonant elements directly correspond to the physical dimensions of the waveguide cavities, with the electrical length of each cavity being close to half of the guided wavelength at the center frequency. In this way, the abstract lumped-element prototype is mapped into a distributed waveguide resonator structure.

The physical realization of the bandpass filter is implemented using iris-coupled waveguide cavities. Each cavity acts as a resonator, while adjacent resonators are electromagnetically coupled through inductive or

capacitive irises etched on the common waveguide wall. The frequency response of the filter is determined, mainly, by the lengths l_i, of the cavities and the sizes d_i of the iris openings, as shown in Fig. 2. A larger iris results in stronger coupling and a wider bandwidth, whereas a smaller iris leads to weaker coupling and narrower bandwidth.

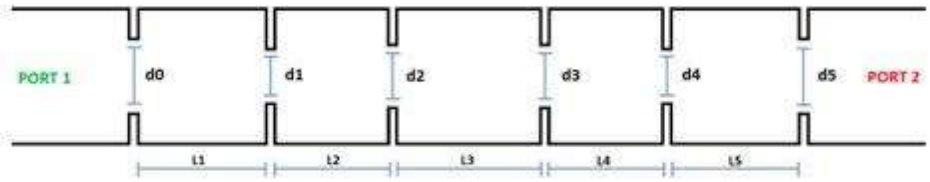

Figure 2. Schematic top view of the 5th-order coupled resonator waveguide filter.

For the analytical design, it has been assumed that a waveguide filter can be viewed as a series of shunt inductors between two transmission lines. The coupling irises are then modeled as shunt susceptance B_k:

$$B_1 = \left(1 - \frac{\omega R}{g_1}\right) / \sqrt{\frac{\omega R}{g_1}} \tag{3}$$

$$B_k = \left(\frac{1}{\omega}\right) \left(1 - \frac{\omega^2}{g_1 g_{k-1}}\right) / \sqrt{g_1 g_{k-1}} \tag{4}$$

$$B_N = \left(1 - \frac{\omega R}{g_{N-1}}\right) / \sqrt{\frac{\omega R}{g_{N-1}}} \tag{5}$$

$$R = 2k^2 + 1 - \sqrt{4k^2 (1 + k^2)} \tag{6}$$

Where $k = 10^{L_{Ar}/10} - 1$, $\omega = \frac{\pi}{2} (\beta_2 - \beta_1) / \beta_0$. L_{Ar} is the passband ripple. The dispersion relation of a waveguide mode is given by $\beta_j = \sqrt{k_j^2 - k_c^2}$, where $k_j = 2\pi f_j \sqrt{\mu\varepsilon}$ is the free-space wavenumber of the mode and $k_c = \pi / \omega_0$ is the cutoff wavenumber. The element values g_i that were used are defined for a LP prototype filter with a N-th order Chebyshev response and a passband ripple of 0.5 (See table 1).

The coupling coefficients $C_{i,i+1}$, which are later used to extract the physical size of the iris openings, are calculated as shown in equation below:

$$C_{i,i+1} = \frac{BW}{f_0} \sqrt{\frac{1}{g_i g_{i+2}}} \tag{7}$$

where BW is the bandwidth of the filter and f_0 is the center frequency of the passband. The physical length of each resonator is related to its electrical length $\emptyset$ as shown in Eq. (8):

$$l_i = \frac{\emptyset_i}{\pi} \frac{\lambda_{g0}}{2} \tag{8}$$

where $\lambda_{g0} = 2\pi / \beta_0$. The electrical length is given by Eq. (9).

$$\emptyset_i = \pi - \frac{1}{2}\left(arctan\ arctan\ \frac{2}{B_{i+1}} + arctan\ arctan\ \frac{2}{B_i}\right) \quad (9)$$

The remaining task is to extract the physical dimensions of the iris openings d_i. Consider a circuit composed of two coupled resonators with resonant frequency . It can be shown that when the symmetry plane of the circuit is replaced by a short circuit, the coupling coefficient is modified, resulting in a lower resonant frequency f_e. Conversely, replacing the symmetry plane with an open circuit increases the resonant frequency to f_m. The relationship between the coupling coefficient and the shifted resonant frequencies is given by Eq. (10):

$$C_{i,i+1} = \frac{f_e^2 - f_m^2}{f_e^2 + f_m^2} \quad (10)$$

For two waveguide resonators coupled through an iris opening, the short-circuit condition is equivalent to introducing a wall with a perfect electric conductor (PEC) boundary condition across the width of the iris. Similarly, the open-circuit condition corresponds to inserting a perfect magnetic conductor (PMC) wall at the iris. To determine the appropriate iris opening widths for the waveguide filters, Eq. (10) is employed in conjunction with CST simulations. Two waveguide resonators coupled by an iris are simulated with a PEC and a PMC wall, respectively, spanning the width of the iris opening. For each case, the corresponding resonant frequencies are calculated while the iris width is incrementally varied. The coupling coefficient is then extracted by substituting the two resonant frequencies into Eq. (10), and the resulting values are plotted as a function of the iris width. The required iris opening widths d_i for the filters are subsequently obtained graphically or by interpolation from the resulting curves. Based on these theoretical calculations, an initial filter design is obtained, which is further optimized using CST to achieve the final design meeting the specified performance requirements.

Section 3: 100 - 110 GH attempt for CTS Diagnostics

The image rejection filter is designed to satisfy the stringent requirements of the W-band millimeter-wave diagnostic receiver. The target passband is specified as 100 - 110 GHz with an insertion loss better than 1 dB, while a high rejection level is required at the image frequency. In particular, the rejection depth at 96 GHz is required to be over 30 dB to effectively suppress the image-band interference.

Based on the theoretical synthesis described in Sec. II, a sixth-order Chebyshev bandpass filter is sufficient to meet the above performance requirements, providing a good trade-off between passband flatness, out-of-band rejection, and fabrication complexity. Therefore, a sixth-order waveguide bandpass filter topology with WR-10 waveguide is adopted in this work. Using the low-pass to bandpass transformation and the iris-coupled resonator model introduced in Sec. II, the initial physical dimensions of the resonators and irises are extracted analytically. These initial dimensions are then imported into CST Microwave Studio [32] for full-wave electromagnetic optimization. The optimization targets include the passband insertion loss, return loss, and the rejection depth at the image frequency. The final optimized geometric parameters of the filter are

summarized in Table II. Figure 3 shows the three-dimensional model of the optimized filter structure. The filter is implemented in a standard rectangular waveguide configuration with six cascaded resonant cavities coupled by irises.

Table II. Detailed dimension of the W-band 100 – 110 GHz filter after optimization.

	l_1	l_2	l_3	l_4	l_5	l_6	**S/L**
Value (micron)	1286	1450	1476	1476	1450	1286	2000
	d_0	d_1	d_2	d_3	d_4	d_5	d_6
Value (micron)	1271	964	899	902	899	964	1271

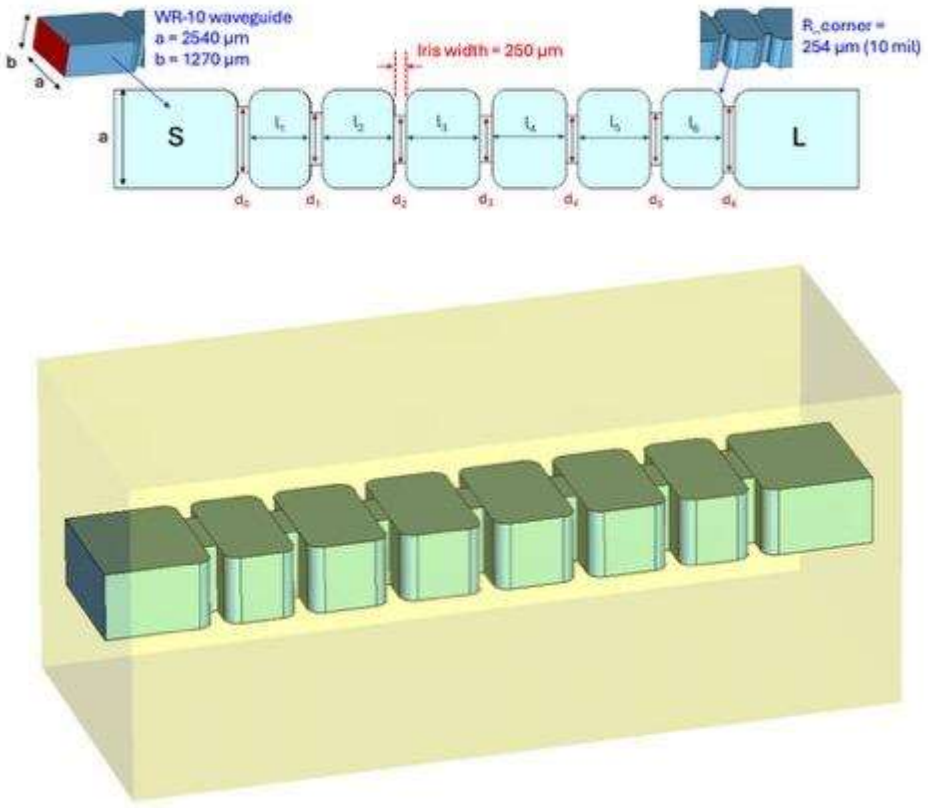

Figure 3. Two-dimensional (up) and three-dimensional (down) views of the proposed six-order waveguide image rejection filter used for electromagnetic simulation and fabrication.

In the numerical simulations, the practical fabrication material is considered. The filter body is modeled using Aluminum Alloy 2024-T4/T6 with an electrical conductivity of $1.734 \times 10^7\ S/m$, which is consistent with the material used in the actual machining process. Figure 4 presents the simulated scattering parameters of the optimized filter. The filter exhibits a flat passband covering 100–110 GHz with an insertion loss better than 1 dB. Meanwhile, a deep rejection is achieved at 96 GHz with > 40 dB rejection depth, satisfying the image rejection requirement for the diagnostic receiver module.

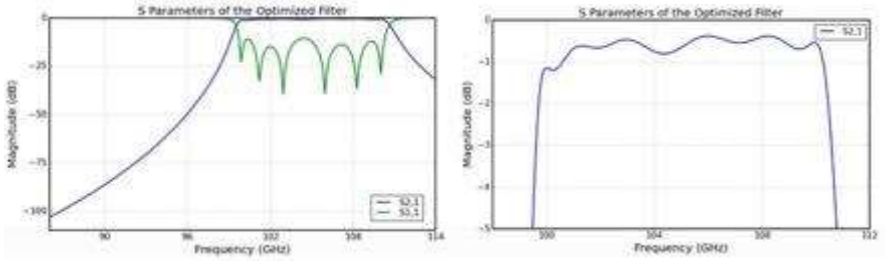

Figure 4. Simulated S-parameters of the optimized image rejection filter, demonstrating a strong rejection at the image frequency (left) and low insertion loss in the 100 –110 GHz passband (right).

To evaluate the robustness of the filter performance against fabrication imperfections, a comprehensive tolerance analysis is carried out by introducing dimensional perturbations to the optimized design. Two major types of fabrication errors are considered. The first type is the variation of the waveguide height parameter b, which is scanned from 1,260 μm to 1,280 μm to reflect possible deviations during machining. The simulation results indicate that variations in b within this range do not cause any significant degradation in the filter performance, including the passband insertion loss and the image-band rejection.

The second type of tolerance analysis focuses on the dimensional variations of the resonator lengths and iris widths, which are more critical to the filter response. A systematic parameter shift d_{shift} is introduced to the key dimensions, including l_m (m = 1, 2, 3, 4, 5), and d_n (n = 0, 1, 2, 3, 4, 5, 6). Meanwhile, the iris widths are adjusted in a complementary manner: when d_{shift} is increased, the first and last iris widths are decreased by 0.5 d_{shift}, and all other iris widths are decreased by d_{shift}; when d_{shift} is decreased, the first and last iris widths are increased by 0.5 d_{shift}, and all other iris widths are increased by d_{shift}. The scanning range of d_{shift} is from −10 μm to +10 μm. The tolerance analysis results show that when d_{shift} is small, the filter performance remains close to the nominal design. However, when d_{shift} becomes relatively large, noticeable degradation occurs, including a clear shift of the passband center frequency. In extreme cases, the passband may shift outside the target range of 100 -110 GHz, causing the filter to no longer meet the design specifications, as shown in Figure 5. These results indicate that the performance of the proposed filter is highly sensitive to the combined dimensional errors of the cavity lengths and iris widths.

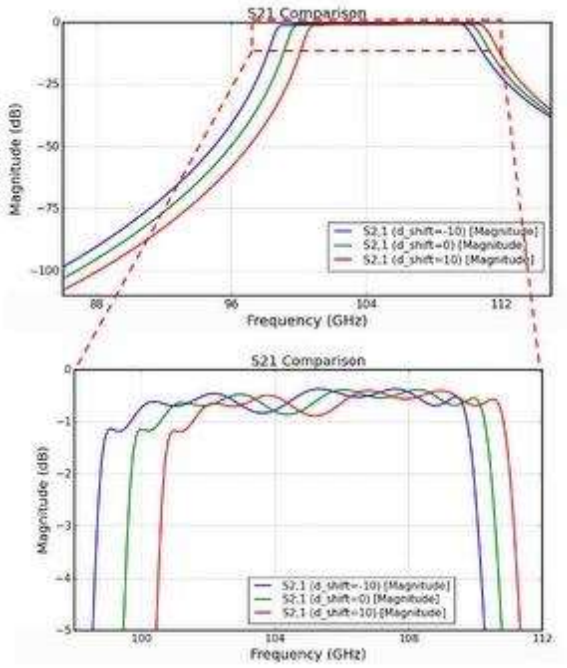

Figure 5. Simulated scattering parameters of the optimized filter for fabrication tolerance analysis with $d_{shift} = \pm 10$ microns, showing the induced passband frequency shift and performance degradation under large dimensional errors.

Based on the above analysis, it is necessary to carefully control the fabrication accuracy in the practical manufacturing process. After machining, the actual physical dimensions of the filter should be measured precisely, and iterative adjustments of the machining parameters are required to compensate for systematic deviations. Through this approach, the final fabricated filter can be ensured to meet the desired electrical performance of the image rejection filter for millimeter-wave diagnostics.

Section 4: 127 - 143 GHz attempt for W7-X Diagnostics

While previous work has demonstrated the successful implementation of iris-coupled waveguide filters at W-band frequencies, the extension to D-band poses additional challenges related to dimensional scaling, fabrication tolerances, and conductor losses.

An eighth-order Chebyshev bandpass filter operating in the 127–145 GHz range is designed for W7-X diagnostic applications. The transition from W-band to D-band is achieved by replacing the WR-10 waveguide with a WR-6 waveguide, with dimensions 1.651 mm × 0.8255 mm, ensuring single-mode operation over the 110 – 170 GHz frequency range. The filter consists of eight cascaded half-wavelength resonant cavities coupled by capacitive irises in a symmetric configuration which is similar with the one mentioned in Section 3. A 0.5 dB ripple Chebyshev prototype is adopted. The initial iris openings and cavity lengths are calculated using theory in

Section 2. The analytical dimensions provide an effective starting point for numerical optimization, with typical deviations of 15 – 20% from the final optimized values.

The filter is modeled using Aluminum Alloy 2024-T4/T6, with conductivities of $1.734 \times 10^7\ S/m$, respectively. Full-wave optimization is carried out to refine the dimensions by accounting for higher-order mode interactions, evanescent field effects, fillet radii, iris thickness, and realistic material properties. The final optimized dimensions of the copper filter are summarized in Table III.

Table III. Detailed dimension of the D-band 127 – 143 GHz filter after optimization.

	l_1	l_2	l_3	l_4	l_5	l_6	l_7	l_8	**S/L**
Value (micron)	1027	1114	1169	1175	1175	1169	1114	1027	2000
	d_0	d_1	d_2	d_3	d_4	d_5	d_6	d_7	d_8
Value (micron)	1123	884	810	795	790	795	810	884	1123

The simulated frequency response of the optimized copper filter exhibits a passband covering 127–145 GHz with a maximum insertion loss of approximately 1.0 dB. A rejection level exceeding 40 dB is achieved at 123 GHz, and the passband ripple is about 0.75 dB, fully satisfying the target specifications as shown in Fig. 8.

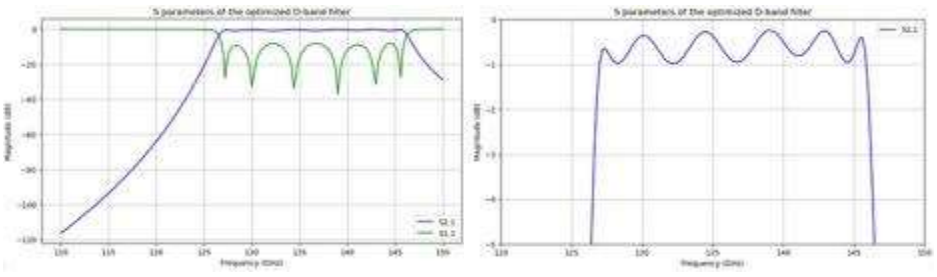

Figure 6. Simulated scattering parameters of the optimized D-band filter using Aluminum Alloy 2024-T4/T6 as the conductor material, showing the stopband (left) and passband (right) performance over the frequency range of interest.

Section 5: Summary

This work successfully addresses this critical challenge through the development and validation of a compact, high-performance W-band (100–110 GHz) filter. Specifically, a 6th-order Chebyshev coupled-resonator waveguide filter was designed, fabricated, and tested for the Collective Thomson Scattering (CTS) receiver system. The laboratory measurements confirmed the success of the design, showing a flat passband of 100 – 110 GHz (Insertion Loss < 1 dB) and achieving the required rejection depth > 40 dB in the image band (86–96 GHz). Furthermore, the design methodology was proven to extend robustly to higher frequencies. We presented the premium design of an 8th-order Chebyshev D-band (127–145 GHz) filter suitable for next-generation diagnostics, such as those used in the W7-X stellarator. Simulated results confirmed that this scaled design achieves comparable performance metrics, including a high rejection level. This established scalability underscores the viability of the proposed solution for integration with radiation-hardened receivers on advanced fusion reactors, providing a necessary and future-proof component for maintaining signal integrity in extreme environments.

ACKNOWLEDGEMENTS

This work is supported by the US Department of Energy under US DoE grant DE-FG02-99ER54531.

DATA AVAILABILITY

The data that support the findings of this study are available from the corresponding author upon reasonable request.

REFERENCES

[1] Ovsyannikov, A. A., and Mikhail Fedorovich Zhukov, eds. Plasma diagnostics. Cambridge Int Science Publishing, 2000.

[2] Y. Li, et al., "Upgrade of the multi-energy soft x-ray diagnostic system for studies of ELM dynamics in the EAST tokamak." Fusion Engineering and Design 137, 414-419 (2018).

[3] Q. Yang, et al., " Combined Langmuir-magnetic probe measurements of type-I ELMy filaments in the EAST tokamak." Plasma Science and Technology 20 (6), 065101 (2018).

[4] X. Li, et al. "Development of ultra-short pulse reflectometry on the Experimental Advanced Superconducting Tokamak (EAST)." Review of Scientific Instruments 95, 073519 (2024).

[5] P. Sun, et al., "Millimeter-wave high-wavenumber scattering diagnostic developments on EAST and NSTX-U", Review of Scientific Instruments 95, 083553 (2024).

[6] Deng, B. H., et al. "THz techniques in plasma diagnostics." 2002 IEEE MTT-S International Microwave Symposium Digest (Cat. No. 02CH37278). Vol. 3. IEEE, 2002.

[7] Li, X.L., Liu, Y., Xu, G.S., Zhou, T.F. and Zhu, Y.L., 2021. Design and characterization of a single-channel microwave interferometer for the Helicon Physics Prototype eXperiment. *Fusion Engineering and Design*, *172*, p.112914.

[8] Domier, C.W., Zhu, Y., Pereira, R.J., Steer-Furderer, J., Li, X., Chen, R., Xu, G., Sun, P. and Luhmann, N.C., 2022. Ultrashort Pulse Reflectometry (USPR) diagnostic for EAST. *Journal of Instrumentation*, *17*(02), p.C02010.

[9] Y. Zhu, et al., "System-on-chip approach microwave imaging reflectometer on DIII-D tokamak." Review of Scientific Instruments 93.11 (2022): 113509.

[10] Li, X.L., Zhu, Y.L., Yu, G.Y., Cao, J.H., Xu, G.S. and Luhmann, N.C., 2021. High level of integration of front-end imaging optics system for electron cyclotron emission imaging diagnostics on the DIII-D tokamak. *Fusion Engineering and Design*, *172*, p.112915.

[11] G. Yu, et al., "Diagnosing the pedestal magnetic field and magnetohydrodynamics radial structure with pedestal–scrape of layer electron cyclotron emission radiation inversion in H-mode plasma." Review of Scientific Instruments 93.10 (2022).

[12] Zhu, Y., Yu, J.H., Yu, G., Ye, Y., Tobias, B., Diallo, A., Kramer, G., Ren, Y., Domier, C.W., Li, X. and Luo, C., 2020. W-band system-on-chip electron cyclotron emission imaging system on DIII-D. *Review of scientific instruments*, *91*(9).

[13] Yu, G., Kramer, G.J., Zhu, Y., Li, X., Wang, Y., Diallo, A., Ren, Y., Yu, J.H., Chen, Y., Liu, X. and Cao, J., 2021. Noise suppression for MHD characterization with electron cyclotron emission imaging 1D technique. *Plasma Physics and Controlled Fusion*, *63*(5), p.055001.

[14] Chen, Jie, et al. "Faraday-effect polarimeter diagnostic for internal magnetic field fluctuation measurements in DIII-D." Review of Scientific Instruments 87.11 (2016).

[15] Sun, Pengjun, et al. "Development and Preliminary Results of 270 GHz Microwave Forward Scattering Diagnostic System on the Experimental Advanced Superconducting Tokamak (EAST)." Plasma Physics and Controlled Fusion (2025) 67 085029.

[16] Y. Zhu, et al., "System-on-chip upgrade of millimeter-wave imaging diagnostics for fusion plasma." Review of Scientific Instruments 92.5 (2021).

[17] Li, Xiaoliang, et al. "System-on-chip Technology Application on Microwave Imaging Reflectometer." *Plasma Physics and Controlled Fusion* (2025).

[18] X. Li, et al., "GaN-based W-band receiver chip development for fusion plasma diagnostics." Journal of Instrumentation 19 P06046 (2024).

[19] X. Yu et al, "Numerical simulation of ultrashort-pulse reflectometry (USPR) on EAST." Plasma Sci. Technol., 25 (2023) 125601.

[20] G. Yu, et al. "Modelling of the electron cyclotron emission burst from a laboratory tokamak plasma with loss-cone maser instability." *Journal of Plasma Physics* 90.6 (2024): 985900601.

[21] Li, Xiaoliang, et al. "Electron Cyclotron Emission–Based Separatrix Identification in ITER with OMFIT Synthetic Modeling." Fusion Science and Technology (2025): 1-9.

[22] G. Yu, et al. "Modeling the electron cyclotron emission radiation signature from suprathermal electrons in a tokamak." Review of Scientific Instruments 95, 073505 (2024).

[23] Churchill, R.M., Tobias, B., Zhu, Y. and DIII-D team, 2020. Deep convolutional neural networks for multi-scale time-series classification and application to tokamak disruption prediction using raw, high temporal resolution diagnostic data. *Physics of Plasmas*, *27*(6).

[24] Choi, W., La Haye, R.J., Lanctot, M.J., Olofsson, K.E.J., Strait, E.J., Sweeney, R., Volpe, F.A. and DIII-D Team, 2018. Feedforward and feedback control of locked mode phase and rotation in DIII-D with application to modulated ECCD experiments. *Nuclear Fusion*, *58*(3), p.036022.

[25] Li, Xiaoliang, et al. "The Dual-Electron Cyclotron Emission Based Measurement of 3D Structures on DIII-D Tokamak." Plasma Physics and Controlled Fusion (2025).

[26] Bin, W., Bruschi, A., D'Arcangelo, O., Castaldo, C., De Angeli, M., Figini, L., Galperti, C., Garavaglia, S., Granucci, G., Grosso, G. and Korsholm, S.B., 2015. First operations with the new Collective Thomson Scattering diagnostic on the Frascati Tokamak Upgrade device. *Journal of Instrumentation*, *10*(10), p.P10007.

[27] Asayama, Shin'ichiro, et al. "A novel compact low loss waveguide image rejection filter based on a backward coupler with band pass filters for 100 ghz band." Journal of Infrared, Millimeter, and Terahertz Waves 36.5 (2015): 445-454.

[28] S. Qiu, et al., " Design of a 140 GHz waveguide notch filter for millimeter-wave receiver module protection in fusion plasma diagnostics.", Rev. Sci. Instrum. 95, 023503 (2024).

[29] Luo, Chen, et al. "Design of the High-Q Approach Notch Filter for 60 GHz Collective Thomson Scattering System." Plasma Science and Technology (2025).

[30] Pozar, David M. Microwave engineering: theory and techniques. John wiley & sons, 2021.

[31] G. L. Matthaei, I. Young, and E. M. T. Jones, Microwave Filters, Impedance-Matching Networks, and Coupling Structures (Dedham, Mass. : Artech House, 1980).

[32] Dassault Systèmes, 2024. CST Studio Suite. Available at: <https://www.3ds.com/products-services/simulia/products/cst-studio-suite/>.

[33] L. Himes, et al., "The 140 GHz notch filter development for millimeter-wave diagnostics protection on the stellarator Wendelstein 7-X." Journal of Instrumentation 19 P10024 (2024).